3-D Full-Wave Inversion of Helicopter Transient Electromagnetic Data in Frequency Domain

Chen Qiu, Bingyang Liang, Feng Han, *Member, IEEE*, Jutao Li, Guangyou Fang, and Qing Huo Liu, *Fellow, IEEE*

***Abstract*— Helicopter transient airborne electromagnetics (HTEM) has become a useful tool in mineral explorations and geological or environmental detection in recent decades. This article presents the frequency-domain 3-D full-wave inversion of the electromagnetic data recorded by a newly built HTEM system. In the forward process, the secondary magnetic field is calculated through the volume electric-field integral equation (EFIE). In the inversion process, the secondary field is first extracted from the total field measured by the HTEM system. Then the Born iterative method (BIM) is adopted to solve the nonlinear inverse scattering problem for the 3-D reconstruction of conductivity. It is first applied to the synthetic models to verify their effectiveness and accuracy. The effects of adjacent underground anomalies on the 3-D inversion performed in a local region within the long flight lines are studied and discussed. Then the BIM solver is used to invert for the underground anomalies using the field measured data recorded by the newly built HTEM system. The 2-D slices from the reconstruction are compared with the nomogram. It is found that the locations of the high-conductivity regions in the BIM results are consistent with locations of the peaks in the nomogram. The reconstructed profiles are also compared with the drilling data obtained near one flight line. The good agreement shows that the 3-D BIM inversion algorithm can be used to reconstruct the underground ore in HTEM surveys.**

***Index Terms*— Electric-field integral equation (EFIE), frequency-domain inversion, helicopter transient electromagnetics (HTEM), nomogram.**

I. Introduction

OVER the past 70 years, the airborne electromagnetics (AEM) has been successfully applied to surveying geological structures for mineral exploration, groundwater surveillance, geological conductivity mapping, environmental monitoring, etc., [1]–[4]. The airborne platform has an overwhelming advantage for surveying large-scale areas rapidly with low costs [5], [6] since the transmitter and receiver coils usually move synchronously in an AEM system. Boosted by the technological development and commercial needs, the AEM system gradually evolved into two types of platforms, fixed-wing, and helicopter-borne [7]. Both of them can be used to investigate underground structures in time domain or frequency domain. The fixed-wing AEM system, which employs a high-moment, wide-band transmitter, and separated receiver coils, is suitable for surveying large areas and detecting deeper regions [8]. On the other hand, a helicopter-borne electromagnetic (HEM) survey system uses low-moment, narrowband transmitter and closely spaced receivers with a rigid frame between the transmitter and receiver coils [8]. A frequency-domain HEM system can offer high resolution and excellent conductivity discrimination for shallow surface imaging. But a time-domain HEM system can perform deeper investigation than a frequency-domain system [9].

Over the last decades, various data interpretation methods for AEM systems have been developed and applied to field data [10]. In the beginning, AEM data were interpreted by carrying out conductivity-depth imaging (CDI) or 1-D inversion for a layered earth model because they are fast for engineering applications. However, the reconstructed profiles by these 1-D methods usually show distribution with discontinuities, and are not reliable if the survey area has complex underground structures. On the other hand, multidimensional inversion has high computational burden because Maxwell's equations must be solved for each transmitter. This dramatically increases the computational cost if we adopt 3-D instead of 1-D inversion of AEM data.

Researchers have proposed several algorithms to improve the computational speed and reduce the memory requirement for 3-D data interpretation of AEM surveys. The inversion algorithms for an AEM system mainly depend on the field data acquisition methods. For a time-domain AEM system, the measured late-time B-field or dB/dt data are usually used to fit model simulated results. Therefore, the inversion is always performed in the time domain. However, the forward computation can be carried out in both the time domain and frequency domain. For the time-domain computation, the whole inversion domain is discretized, and sophisticated numerical solvers are adopted to simulate the total magnetic field at the receivers. For example, Wilson *et al.* [11] applied the finite-element method to calculate 2.5-D geoelectrical models for AEM surveys. In [12], the large-scale 3-D EM

Manuscript received June 11, 2019; revised August 16, 2019 and December 7, 2019; accepted January 20, 2020. Date of publication February 10, 2020; date of current version June 24, 2020. This work was supported by the National Key Research and Development Program of the Ministry of Science and Technology of China under Grant 2018YFC0603503 and Grant 2018YFF01013300. *(Corresponding authors: Feng Han; Qing Huo Liu.)*

Chen Qiu, Bingyang Liang, and Feng Han are with the Institute of Electromagnetics and Acoustics, Fujian Provincial Key Laboratory of Electromagnetic Wave Science and Detection Technology, Xiamen University, Xiamen 361005, China (e-mail: feng.han@xmu.edu.cn).

Jutao Li and Guangyou Fang are with the Institute of Electronics, Chinese Academy of Sciences, Beijing 100190, China (e-mail: gyfang@mail.ie.ac.cn).

Qing Huo Liu is with the Department of Electrical and Computer Engineering, Duke University, Durham, NC 27708 USA (e-mail: qhliu@duke.edu).

Color versions of one or more of the figures in this article are available online at http://ieeexplore.ieee.org.

Digital Object Identifier 10.1109/TGRS.2020.2968804

problem was solved by using the staggered grid finite difference method. Oldenburg *et al.* [13] used the finite volume technique to formulate the 3-D forward model and calculate the response of conductivity for the time-domain AEM system. By contrast, for the frequency-domain forward computation, the moving footprint technique is always used to save memory cost and improve the computational speed. The whole inversion domain is divided into a series of subdomains. Each subdomain corresponds to each transmitter above it. The calculation of the forward scattering is implemented independently for each transmitter. In the inversion, the Jacobian matrices of all subdomains are assembled to form a sparse matrix which is transformed to its time-domain expression by the inverse Fourier transform. This moving footprint technique was proposed by Cox *et al.* in [14] and tested by Liu and Yin [15] for the multipulse airborne transient EM data inversion. It has the advantage of saving memory in the forward computation. However, the extra model weighting matrix must be evaluated in the inversion [15], [16].

Because the above-discussed inversions [11]–[15] are all performed in the time domain by fitting the recorded decaying curve when the transmitting signals are shut off, the underground shallow region cannot be detected. However, if the inversion is also carried out in the frequency domain, the resolution of shallow region images can be improved. This was accomplished by a frequency-domain AEM system [17]. The frequency-domain inversion of AEM data is limited by the data acquisition methods. As described in [1], the frequency-domain AEM system usually uses a limited number of sampling frequencies for detection and data interpretation, which contains less information than a time-domain system.

If the signals of a time-domain AEM system are recorded in the full transmitted cycle, the inversion can also be performed in the frequency domain. In this way, the transient AEM signals can be used to reconstruct the underground shallow region. This broadband frequency-domain technique has been successfully used in our previous work to reconstruct the conductivity profiles for the underground 1-D or 3-D structures. Both the forward and inversion computations are performed in the frequency domain. The forward problem is formulated in the form of a volume electric field integral equation (EFIE). The whole computational domain is discretized, and several fast solvers [18]–[20] can be adopted to solve it. In this article, we use the stabilized biconjugate gradient fast Fourier transform (BCGS-FFT) to compute the scattered field at the receivers [21]. In the inversion, Born iterative method (BIM) [22] or distorted BIM (DBIM) [23], [24] are used to update the model parameters. Compared with previous frequency-domain inversion methods [15], [25], there is no need to calculate the weighting matrix since the forward computation is performed in the whole inversion domain instead of a series of independent subdomains. In [26], the Fréchet derivatives and DBIM were used for reconstructing the 1-D profiles from data recorded by a grounded airborne transient electromagnetics (GREATEM) system. Later in [27], the BCGS-FFT-BIM was used to reconstruct the underground 3-D profiles from similar data sets. The BCGS-FFT algorithm can maintain the stability of forward modeling in the low-frequency band for the AEM system. In addition, by employing the secondary field extraction technique, we exploit the full-time series data to better reveal the underground structures in the shallow regions.

In this article, the frequency-domain BCGS-FFT-BIM solver is used to reconstruct the conductivity of underground scattering objects from the data recorded by a newly built helicopter-borne transient EM (HTEM) system, CAS-HTEM30, developed by the Institute of Electronics, Chinese Academy of Science (CAS). Compared with our previous work [27], the contribution in this article has the following four different aspects because of the significant differences between HTEM and GREATEM systems: 1) the data preprocess for the BCGS-FFT-BIM solver is different. Specifically, the extraction of the secondary field is different. In the HTEM system, the secondary field is obtained by subtracting the ground response from the measured data since the direct coupling field is canceled by the bucking coil. However, in the GREATEM measurement, the secondary field is acquired by subtracting both the ground response and direct coupling field generated by the line source from the measured data. Here, the direct coupling field means the electromagnetic field radiated by the transmitter and received by the receiver coil without the interference of both the layered ground response and the buried conductivity ore. On the other hand, the primary field in the integral equation usually refers to the direct electromagnetic field radiated by the transmitter and received by the receiver with the interference of the ground response as well as the response of the parallel subsurface layers if there are any in the known background medium. However, it does not include the scattered field caused by the buried conductivity ore. The secondary field in the integral equation means the scattered field in the layered background medium generated by the buried conductivity ore. One point we want to emphasize is that we use the scattered magnetic field to perform the inversion in this work. So the secondary field mainly refers to the scattered magnetic field, and the primary field actually includes the direct coupling field; 2) the reconstruction area is different. Since the transmitter and receiver coils move synchronously in the HTEM measurement, the reconstruction area is much larger than that in the previous GREATEM work as the line source in that system is fixed. In the GREATEM measurement, the reconstruction area is restricted near the line source; 3) in the HTEM measurement, we combine all the transmitter and receiver data together to perform the inversion. The computational cost is much higher than that in the GREATEM measurement since the GREATEM system actually has only one transmitter; 4) the offtime nomogram of HTEM system can be used to validate the reconstructed results of BCGS-FFT-BIM because transmitter and receiver coils move synchronously. On the other hand, the data of GREATEM cannot give the nomogram. Based on the aforementioned differences between HTEM and GREATEM in [27], the implementation of BCGS-FFT-BIM for the reconstruction of HTEM data requires several times of forward computations in each inversion iteration, which leads to a completely different Fréchet derivative matrix in the inverse computation. In addition, because the transmitter and receiver coils move synchronously, the inversion domain

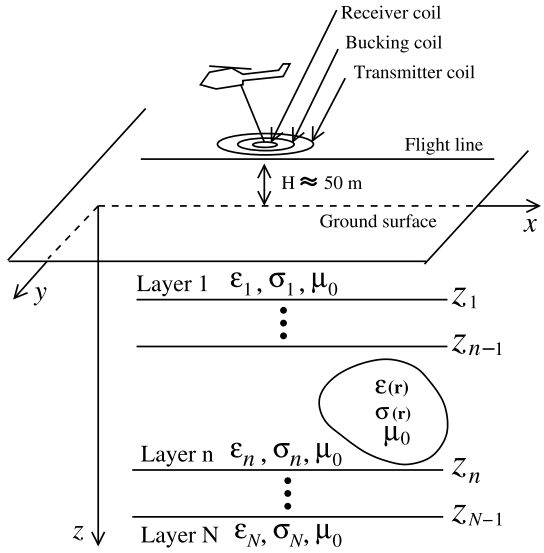

Fig. 1. Geometry for HTEM survey with the anomaly buried in the underground layered medium.

is usually larger than that in the GREATEM measurement, which increases the ill-posedness of the problem. Therefore, we test the feasibility of BIM to perform the local domain inversion with the interference of outside objects for the HTEM measurement. At last, reconstructed results of field data recorded by CAS-HTEM30 are presented to validate the BCGS-FFT-BIM solver for its applications in the HTEM survey.

This article is organized as follows. In Section II, the forward model in the form of EFIE for the HTEM survey and the 3-D inversion method are introduced, and the BCGS-FFT and BIM algorithms are briefly described. The data preprocessing procedure of HTEM is discussed in Section III. The synthetic data are first used to validate the proposed inversion algorithm in Section IV. In Section V, we apply the inversion algorithm to the field measured data recorded by CAS-HTEM30. Finally, conclusions are drawn in Section VI.

II. 3-D Forward Modeling and Inversion Methodology for Airborne Electromagnetics

The brief description of the forward model for EM scattering theory and inversion algorithm for the HTEM survey is presented in this section.

A. 3-D Forward Modeling

Fig. 1 shows the typical configuration of an HTEM survey system. The transmitter and receiver coils are hung by the helicopter at approximately 50 m above the ground. The underground region is divided into several planar layers with the permittivity ϵ_n, conductivity σ_n, and permeability μ_0 in each layer.

In the low-frequency regime, the scattered field $\mathbf{E}_i^{\text{sct}}$ in the ith layer due to the 3-D objects embedded in the nth layer is calculated by

$$\mathbf{E}_i^{\text{sct}} = \left(\mu_0\omega^2 + \frac{j}{\sigma_i}\nabla\nabla\cdot\right)\int_V \mathbf{G}_{\text{in}}^{AJ}(\mathbf{r},\mathbf{r}')\cdot\chi(\mathbf{r}')\mathbf{D}(\mathbf{r}')d\mathbf{r}' \quad (1)$$

where ω is the angular frequency, $\mathbf{D}(\mathbf{r}) \approx -j\sigma_i\mathbf{E}(\mathbf{r})/\omega$ is the electric flux density, and $\mathbf{G}_{in}^{AJ}$ is the magnetic vector potential dyadic Green's function of the layered medium [28]. In (1), χ is the contrast function to parameterize the scattering object

$$\chi(\mathbf{r}) \approx \frac{\sigma(\mathbf{r}) - \sigma_n}{\sigma(\mathbf{r})}. \quad (2)$$

In virtue of the relationship for $\mathbf{E}^{\text{sct}}$, $\mathbf{E}^{\text{inc}}$ and $\mathbf{E}^{\text{tot}}$, we can obtain the EFIE [29]

$$\mathbf{E}_n^{\text{inc}}(\mathbf{r}) = -\frac{\omega}{\sigma_n}\mathbf{D}_n(\mathbf{r}) + (j\omega\sigma_n\mu_0 - \nabla\nabla\cdot) \times \int_V \mathbf{G}_{nn}^{AJ}(\mathbf{r},\mathbf{r}')\cdot\chi(\mathbf{r}')\mathbf{D}_n(\mathbf{r}')d\mathbf{r}'. \quad (3)$$

In (3), $\mathbf{E}^{\text{inc}}$ is the incident field in the computational domain generated by the central loop transmitter in the absence of the target. In the HTEM case, the central loop transmitter can be treated as a magnetic dipole [30]. Using this approximation, $\mathbf{E}^{\text{inc}}$ can be obtained by the dyadic Green's function for each transmitter position as

$$\mathbf{E}^{\text{inc}}(\mathbf{r}) = \int \mathbf{G}^{EM}(\mathbf{r},\mathbf{r}')\cdot\mathbf{M}(\mathbf{r}')d\mathbf{r}' \quad (4)$$

where $\mathbf{M}(\mathbf{r}') = \mu_0\, I\mathbf{S}$ denotes the magnetic dipole source. The I and $\mathbf{S}$ are ring current and vector area of the equivalent central coil. Equation (3) can be discretized and solved efficiently using the fast solver BCGS-FFT. The details can be found in [31] and will not be repeated here.

Once the electric flux density $\mathbf{D}_n(\mathbf{r})$ in (3) inside the computational domain is obtained by BCGS-FFT, the scattered magnetic field $\mathbf{H}^{\text{sct}}$ at the receiver coils can be calculated by

$$\mathbf{H}^{\text{sct}}(\mathbf{r}) = \int_V \mathbf{G}_{\text{in}}^{HJ}(\mathbf{r},\mathbf{r}')\cdot\chi(\mathbf{r}')\mathbf{D}(\mathbf{r}')d\mathbf{r}' \quad (5)$$

where $\mathbf{G}_{\text{in}}^{HJ}(\mathbf{r},\mathbf{r}')$ is the dyadic Green function for the magnetic field in the ith layer due to an electric current source in the nth layer. Its derivation can be found in [28]. The scattered $\mathbf{H}^{\text{sct}}$ is the secondary field which will be used to perform the nonlinear inversion in the HTEM measurement.

B. 3-D Nonlinear Inversion

To reconstruct the conductivity distribution for all sounding locations, we define the following cost function for 3-D inversion of HTEM measured data:

$$F_{m+1}(\chi) = \frac{\|\mathbf{f} - \mathbf{M}_m\cdot\chi_{m+1}\|^2}{\|\mathbf{f}\|^2} + \gamma^2\frac{\|\chi_{m+1}\|^2}{\|\chi_m\|^2} \quad (6)$$

where χ is the vector of model parameters and $\mathbf{M}_m$ is the operator of forward calculation in the mth iteration. This cost function is formulated for the BIM [32], which is suitable for nonlinear inverse scattering problems. In order to obtain a stable solution for the ill-posed problem in the above,

we apply the Tikhonov regularization to the cost function. By minimizing (6), we obtain and solve its equivalent form

$$\left(\frac{\mathbf{M}_m^{\dagger}\mathbf{M}_m}{\|\mathbf{f}\|^2}+\frac{\gamma^2}{\|\chi_m\|^2}\mathbf{I}\right)\chi_{m+1}=\frac{\mathbf{M}_m^{\dagger}\mathbf{f}}{\|\mathbf{f}\|^2} \tag{7}$$

where the superscript † denotes the complex conjugate transposition. The regularization factor γ will slow down the iterative process if it is selected inappropriately for the optimization. In the inversion of HTEM data, we follow the choice given in [33], which has been tested by experimental data. By solving (7) using conjugate gradient (CG) method, we update the model parameters by replacing χ_m with χ_{m+1}. After this, the forward BCGS-FFT algorithm is used to update $\mathbf{D}$ in (3) and thus $\mathbf{M}$ in (6). The whole iterative procedure terminates when the measured data misfit satisfies the stop criterion or the computing program reaches a specified iteration number.

III. HTEM Survey System and Data Preprocessing

In this section, a new helicopter-borne transient system named CAS-HTEM30 designed by the Institute of Electronics, Chinese Academy of Science is briefly introduced. Meanwhile, the preprocessing procedure for the data recorded by this system is given in detail.

The CAS-HTEM30 system adopts the collocated loop geometry. The diameter of the transmitter coil is 30 m while that of the receiver coil is 1.2 m. A bucking coil with the diameter 7.5 m is fixed between the transmitter coil and receiver coil to reduce the direct coupling field at the receiver coil. Three coils are held together by a network of elastic cables. Surrounded by the bucking coil, the 100-turns receiver coil with the gain 100 has an effective area of 11 600 m^2 to record the z component of transient signals during the transmitter on- and off-time. The bucking can reduce the effect of the direct wave from the transmitter. The global position system (GPS) and radar altimeters record the position and altitude of the measurement system and the helicopter, respectively.

The transmitter coil is a four-turn regular hexadecagon, which allows it to reduce the turn-off time of the waveform to less than 600 μs. A waveform with a shorter turn-off time can generate a stronger transient response and helps to enhance the signal-to-noise ratio (SNR) of the received response recorded by the receiver [34]. A bipolar trapezoidal-pulse transient waveform with the peak dipole moment of 186 000 $A \cdot m^2$ is transmitted with a base frequency of 25 Hz. Fig. 2(a) shows the half-cycle of the transmitted waveform employed by the CAS-HTEM30 system. The data sampling rate of the system is 128 kHz and flight velocity is around 90 km/h in the field measurements.

Before interpreting the experimental raw data, a series of preprocessing steps are taken to obtain the frequency-domain high-quality data. The processing procedure includes attitude correction, data stacking, and removal of ground response in spectrum domain.

A. Attitude Correction

During an HTEM survey, the transmitter, receiver, and bucking coils show three types of postures in air, which are the roll, pitch, and yaw, respectively. The transmitted and received signals must be corrected for the posture variations. The CAS-HTEM30 system records the posture data by a gyro during the flight. We use the tri-axis orthogonal coordinate transformation described in [35] to achieve the attitude corrections. The posture of the coil is recorded during on- and off-time, and thus the attitude correction is made for every cycle. Similar procedures have been applied for the GREATEM data in our previous work [27] and details will not be repeated here.

B. Data Stacking

For an HTEM system, data stacking is a necessary technique to suppress the random noise and improve SNR. First, the received signals in the positive and negative half-cycles for a whole transmission cycle are added and averaged to produce a single half-cycle signal. Then the data recorded in each interval of 50 m are averaged and combined to generate one half-cycle transient decay curve. This data sampling interval is consistent with the effective sampling distance given in [25]. We treat this half-cycle signal after data stacking as the sounding data at the middle point of the 50-m covering distance for data interpretation, as shown in Fig. 2(b). The middle point in the 50-m covering distance is called sounding station.

C. Secondary Field Extraction

In the inversion, the scattered magnetic field is used to minimize the cost function. However, the measured data in the HTEM survey system include both the responses of anomalous objects and ground. To extract the scattered field generated by anomalous objects from the measured data, we employ the layered medium Green's functions to calculate the ground response. Different from the previous methods [36], [37], the transmitter loop is treated as the superposition of several small loops with the unit area. The ground response at the center of the transmitter coil or receiver coil is calculated by the summation of the response for each small loop which can be treated as a vertical magnetic dipole [38], [39]. Therefore, it is expressed as

$$\mathbf{H}^z(\mathbf{r})=\sum_{i=1}^{N}\mathbf{G}_i^{HM}(\mathbf{r},\mathbf{r}')\cdot\mathbf{M}_i(\mathbf{r}') \tag{8}$$

where i is the index of the small loop, $\mathbf{G}^{HM}$ is the layered medium Green's function [28], and $\mathbf{M}_i$ is the equivalent magnetic dipole moment of the ith small loop. Once the ground response is obtained, the secondary field is calculated by subtracting it from the measured data, as shown in Fig. 2(c).

IV. Inversion of Synthetic Data

To demonstrate the effectiveness and efficiency of BCGS-FFT-BIM for 3-D inversion of HTEM data, we design two synthetic models to simulate the helicopter-borne EM system described in Section III. The inversion is performed on a workstation with 20-cores Xeon E2650 v3 2.3G CPU, 512-GB RAM.

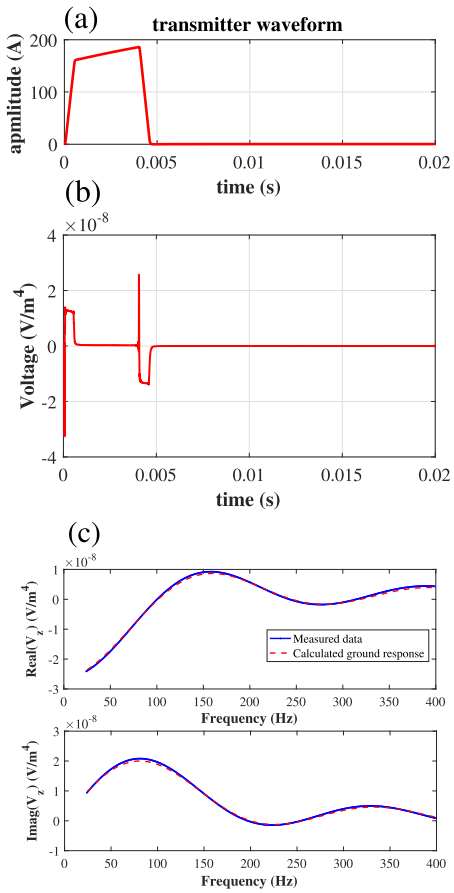

Fig. 2. Signals before and after preprocessing in the CAS-HTEM30 system. (a) Half-period of transmitter waveform. (b) Received signal in the time domain after data processing, which includes attitude correction, data stacking, and normalization. (c) Spectrum comparisons of measured data and calculated ground response without the direct coupling field in the step for secondary field extraction.

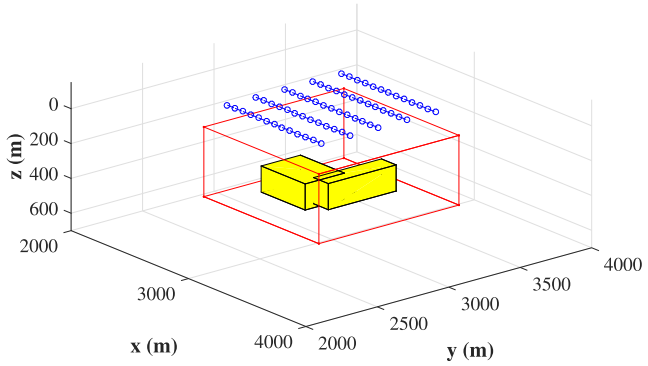

Fig. 3. 3-D synthetic model 1 for helicopter EM survey used to validate the inversion of a single conductive object. Dashed lines: flight lines for HTEM survey and the circle is the sounding location. Red cubic block denotes: forward computational domain. Yellow cubic block: scattering object with "L" shape.

A. Synthetic Model 1

Fig. 3 shows the HTEM survey scheme and computational domain of the synthetic model 1. The background conductivity of the underground region is set as 0.001 S/m. A conductive scattering object with the "L" shape and conductivity

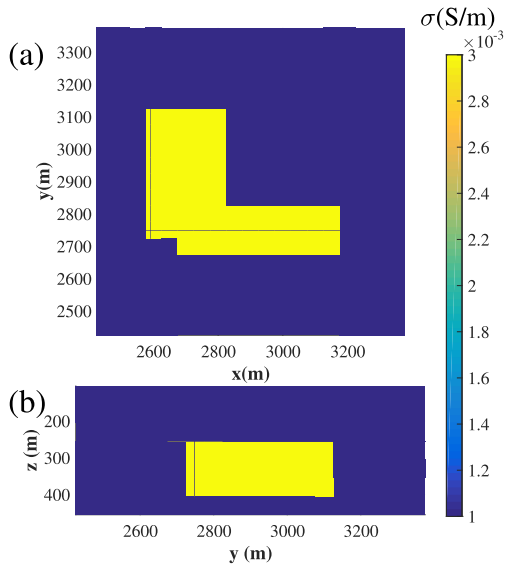

Fig. 4. Location and shape of the conductive object in synthetic model 1. (a) Horizontal slice at the depth of $z = 300$ m. (b) Vertical slice at $x = 2700$ m.

of 0.003 S/m is located in the computational domain. The vertical center of the scattering object is located at $z = 300$ m and the plane view of the object is shown in Fig. 4. The thickness of the object is 150 m and the lengths are 250 and 150 m in the x- and y-direction, respectively. The forward BCGS-FFT solver simulates a helicopter-borne EM survey with 200-m flight line spacing and 50-m inline sounding spacing. The forward computational domain is 1000 m $\times$ 1000 m $\times$ 400 m and there are totally 85 stations of data used for inversion. The flight altitude is 50 m in this simulated survey.

To avoid the "inverse crime" [40] in practical problems, the simulated scattered data are produced by the BCGS-FFT solver using coarse grids, for which the cell number is 20 $\times$ 20 $\times$ 8. In the inversion, the computation is divided into 40 $\times$ 40 $\times$ 16 cells with the grid size of 25 m. This grid size satisfies the criterion that the sampling point in one skin depth is larger than 5 to make both the forward and inversion computation reliable and stable. We contaminate the maximum magnitude of the synthetic secondary field data with -10-dB random white Gaussian noise. The calculation for four frequencies, 25, 145, 500, and 700 Hz, is carried out individually in the forward computation but the synthetic data for all frequencies and 85 sounding stations are assembled together to form the matrix of the cost function in the inversion. We choose this wide sampling frequency band because the low-frequency data and high-frequency data can make up for each other's shortcoming. Low-frequency EM waves can penetrate deeper but only give low-resolution inversion results. By contrast, we can use high-frequency data to obtain high-resolution inversion but only for a shallow-region investigation. Fig. 5(a) shows the variation of data misfits in the iteration procedure. The relative mean-square (rms) data misfit keeps going down stably with the iteration step increasing, and finally approaches 5% in the 30th iteration. This means

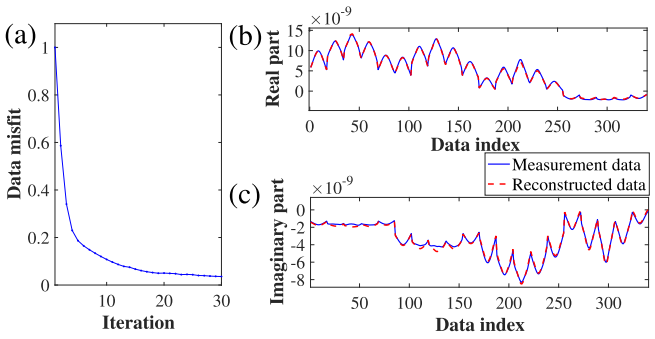

Fig. 5. Variations of rms data misfits in the BIM iteration process. (a) data misfit decreases as the iteration continues. (b) and (c) Real and imaginary parts of data fits of the scattered magnetic fields between simulated measured data and reconstructed data in the last step. The data are arranged for four frequencies with 85 sounding locations in sequence.

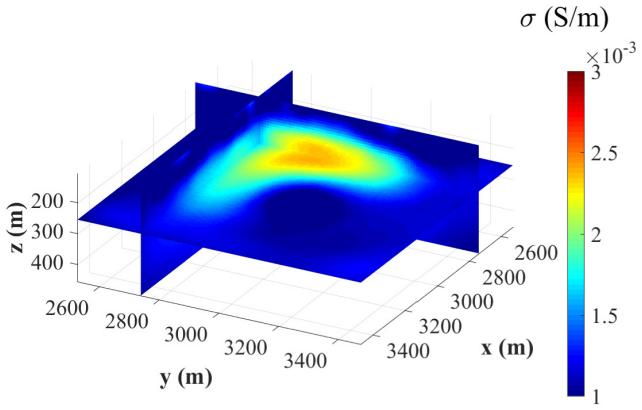

Fig. 6. 3-D reconstructed conductivity profile from synthetic data in model 1.

the iteration procedure is stable using the BIM for inversion. The scattered data fits in the final iteration step are shown in Fig. 5(b) and (c). Because we use four frequencies data collected at 85 different sounding locations, we arrange the data according to the sampling frequency at first. Therefore, when the data index values in Fig. 5(b) and (c) are between 1 and 85, all 85 sets of data are sampled at 25 Hz. But they are arranged for 85 different sounding locations sequentially. In each measurement location, the spectrum of the measured time-domain waveform is sampled at 25 Hz. By comparing the measured data and reconstructed data in the last iteration step, we find that, for different grid sizes, the BCGS-FFT solver performs well in solving 3-D forward EM scattering problems in the low-frequency regime for HTEM measurements.

Fig. 6 shows the 3-D reconstructed conductivity profile. The xy and yz cross sections in Fig. 7(a) and (b) indicate that both the location and the shape of the conductive object can be recovered well by BIM for the HTEM measurements. The reconstructed conductivity of the object is 0.0024 S/m, which is a little smaller than the true value.

B. Synthetic Model 2

Different from the semiairborne survey in which the transmitters are fixed on the ground surface, the transmitter and receiver move synchronously in HTEM survey. Therefore,

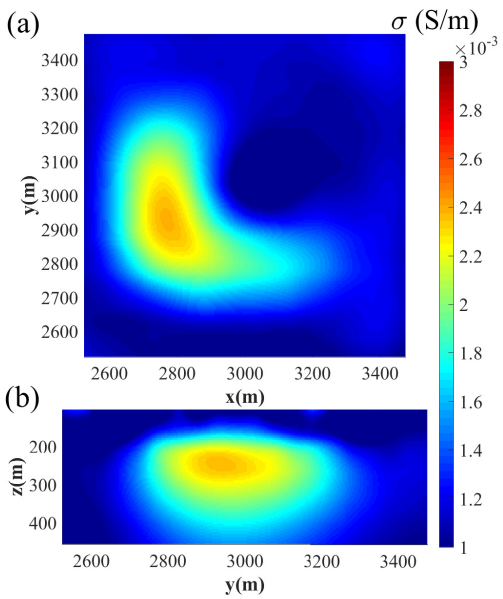

Fig. 7. Slices for the 3-D profiles shown in Fig. 6. (a) Horizontal slice passing through the center of the inversion domain at $z = 300$ m. (b) Vertical slice passing through the center of the inversion domain at $y = 2700$ m.

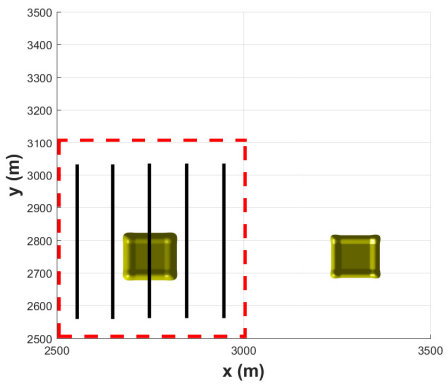

Fig. 8. Scheme of the synthetic model 2 for local inversion from an HTEM survey. Black solid lines: flight lines for the HTEM survey. Red dashed square: local inversion domain.

the flight lines and the survey area have no restriction. On the other hand, the computational domain for the inversion of HTEM data is restricted by computer memory. Therefore, the 3-D inversion can only be performed in the local region for the whole survey area if the flight lines are very long. Because the underground conductive anomalies are usually not isolated, it is necessary to study how the adjacent conductive scatterers affect the inversion performed in a local region.

The model 2 consists of two scattering objects buried underground. The whole calculation domain is 1000 m $\times$ 1000 m $\times$ 400 m and is divided into 50 $\times$ 50 $\times$ 20 cells. The experimental scheme of the HTEM survey for model 2 is shown in Fig. 8. The black solid lines denote the flight lines for forward modeling and the red dashed square represents the local inversion domain for the HTEM data. We use the same receiver's heights as described in the synthetic model 1 but smaller configurations for data sampling and line

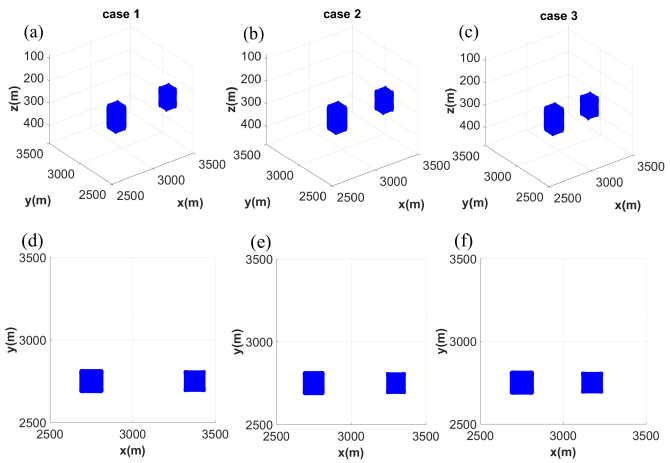

Fig. 9. Three synthetic models used to investigate the feasibility of local inversion for HTEM survey. (a)–(c) 3-D views of the three models. (d)–(f) Plane views at the depth of $z = 150$ m.

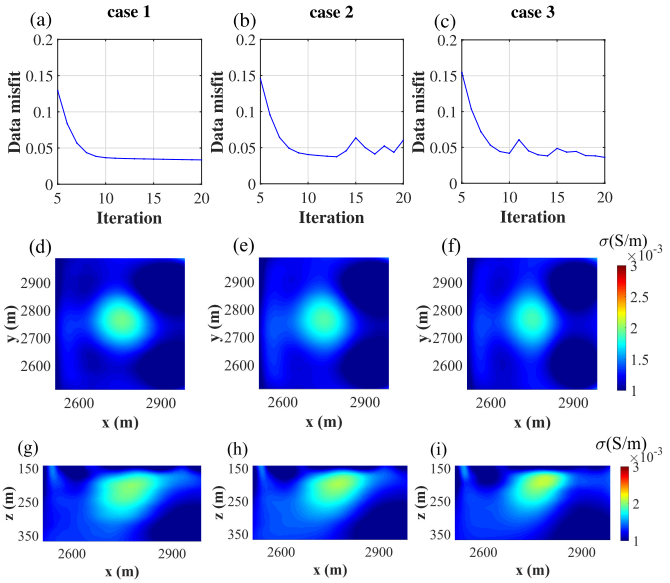

Fig. 10. Data misfits and reconstructed results in three cases when the distance between the outside object and inversion domain is different. (a)–(c) Data misfit curves during iterations. (d)–(f) Horizontal slices at $z = 150$ m for three cases. (g)–(i) Vertical slices at $y = 2750$ m for three cases.

spacing. The flight line spacing is 100 m and inline sounding spacing is 25 m for each flight line. The forward calculation by BCGS-FFT is performed for the whole computational domain. In the inversion, only the data collected in the red dashed square area are used for reconstructing the underground anomaly locally.

To validate the feasibility of the local inversion, we design three different cases for the HTEM measurement. The different locations of two scattering objects in three cases are shown in Fig. 9. The distances between two objects are about 350, 250, and 150 m, respectively. The outside object is located outside the local inversion domain in all three cases. The outside object in case 3 is in the range of "moving footprint" [14], while the objects in cases 1 and 2 are outside the area.

The same sampling frequencies as those in the synthetic model 1 are used in this inversion. The 1000 m $\times$ 1000 m $\times$ 400 m local inversion domain is divided into 50 $\times$ 50 $\times$ 20 cells. The total 85 stations of data are used for reconstructing the underground structure in all three cases. The data misfit curves, the cross sections, and depth slices of the reconstructed results are displayed in Fig. 10. In the inversion, all three cases show stable convergence during the iteration processes. The rms data misfits of cases 2 and 3 show fluctuation in the iteration processes, which means the local inversion is affected by the scattering object outside the computational domain. This is also clearly shown by the plane view at the depth of $z = 150$ m in Fig. 10(d)–(f). Although the reconstructed locations and sizes of the anomaly in the local domain are roughly correct, the shapes of the anomaly are distorted and show fake images when the outside scatterer is closer to the inversion domain. The reconstructed result of case 1 shows the best shape comparing with other two cases for the xy cross sections. As shown in Fig. 10(f) and (i), the scattering object is obviously compressed and affected by the object outside the domain.

From above comparisons, we can conclude that the BCGS-FFT-BIM algorithm can reconstruct the underground anomaly in the local inversion domain, if the distance between the outside object and the local inversion domain satisfies the limited footprint area [25]. This effect is also consistent with the "moving footprint" proposed by Cox *et al.* [14]. This can benefit the data interpretation in HTEM measurements to reduce the computational cost and memory usage.

V. Inversion of Field Measured Data

In 2017, the CAS used the CAS-HTEM30 system and conducted a helicopter-borne time-domain EM survey over the test site on a grassland, located in the north-west of XilinGol League in Inner Mongolia, China. The survey consists of seven flight lines. The location and scheme of the survey are shown in Fig. 11. The red dashed lines denote the flight lines, in which the arrows guide the flying directions of the HTEM system. The survey was performed with the 200-m flight line spacing, covering an area of 9 km $\times$ 1.2 km. The transmitted signal of CAS-HTEM30 system in this survey is a 25 % duty cycle trapezoidal pulse. The base frequency is 25 Hz. In the frequency domain, the measured dB/dt are converted to magnetic field data by dividing $j\omega$. The peak current amplitude of the transmitter loop used in the survey is 186 A. The flight altitude is around 50 m.

The measured data are processed to produce the secondary field in the frequency domain as described in Section III. We tried different values of the underground background conductivity from 0.0001 to 0.001 S/m to calculate the ground response without direct coupling fields. The difference between measured data and calculated ground response reaches the minimum when the underground background conductivity is 0.0003 S/m. For this reason, we use the half-space

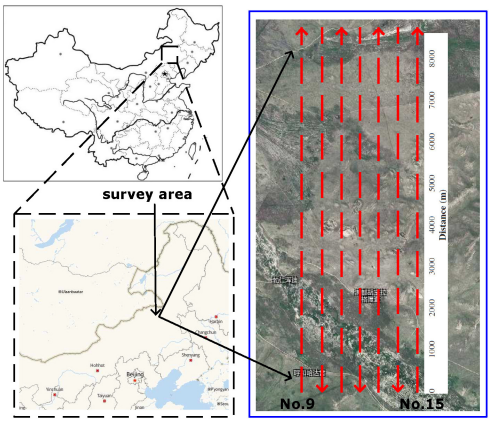

Fig. 11. Maps showing the location and geometry for the CAS-HTEM30 survey conducted in Inner Mongolia, China. Dashed lines: flight lines from No. 9 to No. 15. Arrows of the dashed lines: flight directions.

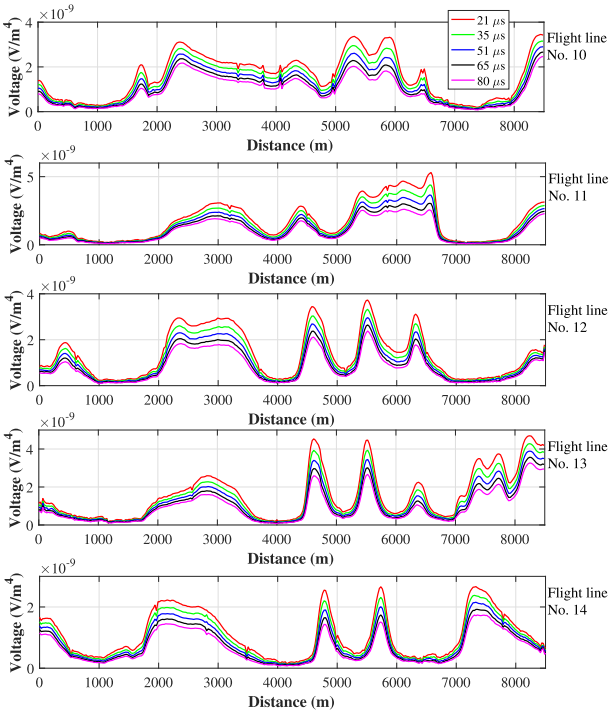

Fig. 12. Offtime nomogram of dB/dt for the 5-channel of CAS-HTEM30 over the flight lines from No. 10 to No. 14 in the survey area. Offtime gate windows are chosen at 21 μs, 35 μs, 51 μs, 65 μs, and 80 μs after current waveform cutoff.

model with background conductivity of 0.0003 S/m as the initial input for the inversion.

To reveal the geological feature of the survey area, we first draw the offtime nomogram of dB/dt for the five channels in five flight lines with directions from south to north. The nomogram includes a series of disjoint lines along different flight lines. An individual nomogram line in a certain flight line shows ground response in different sounding stations after the current waveform of the transmitter coil is cut off. Different nomogram lines have different offtime gate windows. Larger peaks in a nomogram line usually mean conducting objects may exist near the sounding station. As shown in the offtime nomogram in Fig. 12, there exist two peaks of the response from 4400 to 6800 m in the flight line No. 14. The strong offtime response is the characteristic of underground conductive targets. The same phenomenon can be found in lines No. 12 and No. 13, which means the existence of underground anomaly in this area. Considering the data quality and computational cost, we select measured transient responses from 4400 to 6800 m in five flight lines to obtain the local reconstruction for HTEM data.

In this local inversion domain, there are totally 170 sounding stations data used to reconstruct the underground structure. The 3-D computational domain is 2400 m $\times$ 1200 m $\times$ 320 m and discretized into 60 $\times$ 30 $\times$ 8 cells. To save computational time, we divide the whole domain into two identical subdomains. The inversions are performed in two subdomains simultaneously. In the final reconstructed profile, we merge the reconstructed results in two subdomains together and treat it as the reconstructed result for the whole data covering area. Considering the skin depth of the initial input model, we execute the inversion algorithm using four frequencies 45, 250, 450, and 600 Hz. This inversion procedure contains neither geological constraints nor *a priori* geological information. The selection of the background conductivity is based on the data fitting between measured data and ground response, which has been discussed above. We use the same computer as that for the inversion of synthetic models in Section IV, and totally carry out 10 iterations to obtain the reconstructed profile. There are totally 60 000 cells in the inversion domain and 170 sounding stations data. The total computational time is around 3 h. For a practical purpose, this time consumption of the 3-D inversion is tolerable if the results are reliable.

As a local inversion result, the reconstructed 3-D conductivity profile of the survey area from 4400 to 6800 m is shown in Fig. 13. It is obvious that the 3-D reconstruction can provide the information of lateral conductivity distribution between flight lines which is absent in the traditional 1-D inversion. We also compare the spectrum magnitude of the input data measured by the survey system and that of the modeled data reconstructed by BCGS-FFT-BIM in the last iteration step, as shown in Fig. 14. We can see that the input data show obvious fluctuation due to the measurement noise in the experiment. The modeled data show the same general trend as the input data. The rms of data misfit finally approaches 28% in this inversion, which is much larger than that in the synthetic model 1.

Fig. 15 shows the vertical 2-D slices beneath five flight lines for the reconstructed 3-D profile shown in Fig. 13. The most conductive region in the reconstructed results is near the ground surface. In the depth from 150 to 280 m, the conductivity is about 0.0002–0.0004 S/m, which is consistent with both our guess of the underground value 0.0003 S/m used in the initial model and the geological data of 3000–4000 Ω·m provided by CAS. By carefully comparing five vertical slices with the offtime nomogram shown in Fig. 12, we find they have the good match. For example, in all five flight lines when the distance is 4600 m, there is a high conductive

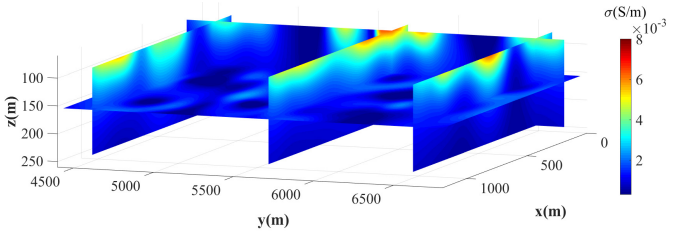

Fig. 13. Reconstructed 3-D conductivity profile from the CAS-HTEM30 field data for the survey area in Fig. 11. The slices perpendicular to the flight line are located at $y = 4600$, 5600, and 6500 m, which are consistent with the peaks in the nomogram in Fig. 12.

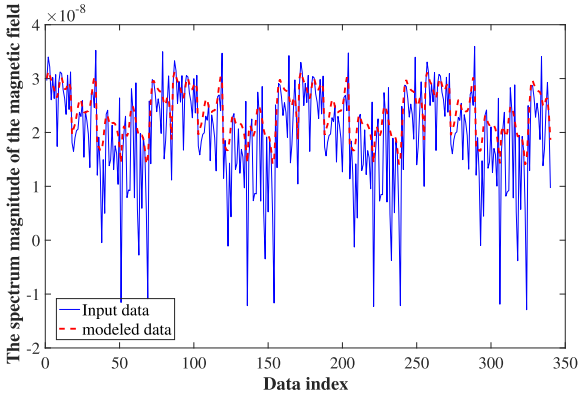

Fig. 14. Comparison between input data measured by the survey system and modeled data reconstructed by BCGS-FFT-BIM in the last iteration step.

anomaly showing up in vertical slices. As shown in the offtime nomogram in Fig. 12, the ground responses in this distance are also larger than the adjacent regions. The amplitudes of response curves in this distance for No. 10 and 11 flight lines are smaller than those for Nos. 12, 13, and 14. This is manifested by the difference of the reconstructed conductivity in this distance shown in five vertical slices. When the distance is 5600 m, the underground regions beneath all five flight lines are highly conductive. In the offtime nomogram, the amplitudes of five ground response curves are all very large. In addition, we notice that the peak amplitude ranges near distance 5600 m are wider in Nos. 10 and 11 in the offtime nomogram curves compared with other three flight lines. Correspondingly, the high-conductivity regions near the distance 5600 m in No. 10 and 11 have wider ranges, which is shown by the reconstructed vertical slices. Near the distance 6600 m, there are conductive anomalies near the underground surface beneath all five flight lines. However, the anomaly beneath flight line No. 14 is very weak, as shown in 2-D slice in Fig. 15. This is consistent with the results in nomogram shown in Fig. 12.

CAS also offers the drilling data near flight line No. 14 in the distance of 5000 m. Fig. 16 shows the comparison of the resistivity values at different depths from the drilling data and BIM inversion. Clearly, the inversion of HTEM measurements by BIM can fit the drilling data well with the increment of depth. These results from CAS-HTEM30 measurements

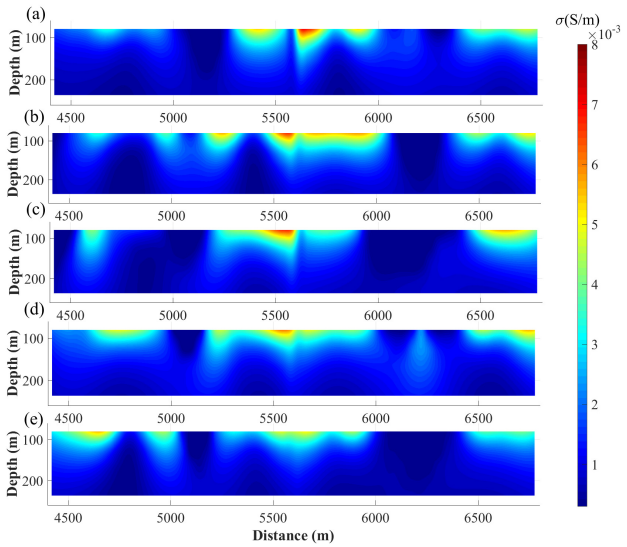

Fig. 15. Vertical 2-D slices beneath five flight lines (a) No. 10 to (e) No. 14 for the 3-D profiles shown in Fig. 13.

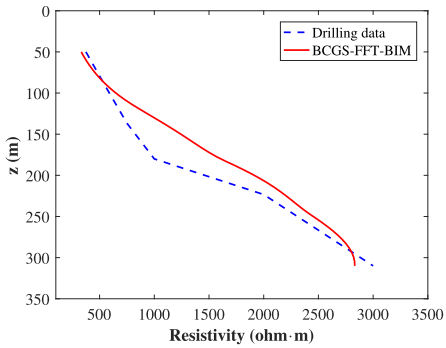

Fig. 16. 1-D transect comparisons of resistivity at different depths in the distance 5000 m near the flight line No. 14.

show a promising application of BCGS-FFT-BIM for data interpretation of an HTEM system.

VI. Conclusion

In this article, the BCGS-FFT-BIM algorithm is used to invert for the underground conductivity distribution from the HTEM data in the frequency domain. Different from the previous frequency-domain inversion method applied to the HTEM data for which the forward computation is performed for a single transmitter and a small subdomain region underground, we directly compute the scattered fields at the receivers generated by the equivalent current in all the discretized cells in the whole computational domain. In the inversion, we adopt the CG method to directly solve the whole matrix equation by using BIM instead of reassembling the Jacobian matrix. To test the inversion algorithm, we use two synthetic models to simulate the HTEM surveys. The algorithm not only can reconstruct a single conductive object located beneath the flight lines, but also works well with a local inversion if the HTEM measurement satisfies the scale of footprint.

We also apply the BIM to the field measured data recorded by the newly built CAS-HTEM30 system, and the survey was

conducted in the Inner Mongolia, China. Before inversion, a series of data preprocessing techniques are applied to obtain the high-quality frequency-domain scattered magnetic field H_z. The spatial distribution of the underground conductive anomalies beneath the flight lines reconstructed by BIM is roughly consistent with the feature shown in the offtime nomogram. The nomogram only gives the qualitative underground ore distribution. By contrast, the BIM full-wave inversion not only provides the 3-D spatial distribution of the ore, but also gives the conductivity values. By comparing with the drilling data near one flight line, we find that the variation of conductivity with depth increment from BIM and drilling matches well. The whole 3-D conductivity profile for the 2400 m $\times$ 1200 m $\times$ 320 m underground region can be obtained within 3 h. This means the BCGS-FFT-BIM can be potentially used to reconstruct the ore distribution reliably in the shallow region of a large area from the HTEM data with reasonable computational cost.

REFERENCES

[1] D. Fountain, "Airborne electromagnetic systems–50 years of development," *Explor. Geophys.*, vol. 29, nos. 1–2, pp. 1–11, Mar. 1998.

[2] L.-P. Song, S. D. Billings, L. R. Pasion, and D. W. Oldenburg, "Transient electromagnetic scattering of a metallic object buried in underwater sediments," *IEEE Trans. Geosci. Remote Sens.*, vol. 54, no. 2, pp. 1091–1102, Feb. 2016.

[3] M. Hallikainen *et al.*, "A helicopter-borne eight-channel ranging scatterometer for remote sensing. I. System description," *IEEE Trans. Geosci. Remote Sens.*, vol. 31, no. 1, pp. 161–169, Jan. 1993.

[4] J. Hyyppa and M. Hallikainen, "A helicopter-borne eight-channel ranging scatterometer for remote sensing. II. Forest inventory," *IEEE Trans. Geosci. Remote Sens.*, vol. 31, no. 1, pp. 170–179, Jan. 1993.

[5] R. S. Smith, A. P. Annan, and P. D. McGowan, "A comparison of data from airborne, semi-airborne, and ground electromagnetic systems," *Geophysics*, vol. 66, no. 5, pp. 1379–1385, Sep. 2001.

[6] J. Macnae, "Developments in broadband airborne electromagnetics in the past decade," in *Proc. Explor.*, 2007, p. 23.

[7] M. Allard, "On the origin of the HTEM species," *Adv. Airborne Geophys.*, vol. 7, no. 21, pp. 355–374, 2007.

[8] S. Balch, "The emerging role of helicopter time domain EM systems," *ASEG Extended Abstr.*, vol. 2004, no. 1, pp. 1–4, Dec. 2004.

[9] B. Siemon, A. V. Christiansen, and E. Auken, "A review of helicopter-borne electromagnetic methods for groundwater exploration," *Near Surf. Geophys.*, vol. 7, nos. 5–6, pp. 629–646, Oct. 2009.

[10] C.-C. Yin, X.-Y. Ren, Y. Liu, Y.-F. Qi, C.-K. Qiu, and J. Cai, "Review on airborne electromagnetic inverse theory and applications," *Geophysics*, vol. 80, no. 4, pp. W17–W31, Jul. 2015.

[11] G. Wilson, A. P. Raiche, and F. Sugeng, "2.5D inversion of airborne electromagnetic data," *Explor. Geophys.*, vol. 37, no. 4, pp. 363–371, Jan. 2006.

[12] G. A. Newman and P. T. Boggs, "Solution accelerators for large-scale three-dimensional electromagnetic inverse problems," *Inverse Problems*, vol. 20, no. 6, pp. S151–S170, Dec. 2004.

[13] D. Yang and D. W. Oldenburg, "Three-dimensional inversion of airborne time-domain electromagnetic data with applications to a porphyry deposit," *Geophysics*, vol. 77, no. 2, pp. B23–B34, Mar. 2012.

[14] L. H. Cox, G. A. Wilson, and M. S. Zhdanov, "3D inversion of airborne electromagnetic data using a moving footprint," *Explor. Geophys.*, vol. 41, no. 4, pp. 250–259, Dec. 2010.

[15] Y. Liu and C. Yin, "3D inversion for multipulse airborne transient electromagnetic data," *Geophysics*, vol. 81, no. 6, pp. E401–E408, Nov. 2016.

[16] Y. Qi, L. Huang, X. Wang, G. Fang, and G. Yu, "Airborne transient electromagnetic modeling and inversion under full attitude change," *IEEE Geosci. Remote Sens. Lett.*, vol. 14, no. 9, pp. 1575–1579, Sep. 2017.

[17] J. W. Goold, "Spectral complex conductivity inversion of airborne electromagnetic data," M.S. thesis, Dept. Geol. Geophys., Univ. Utah, Salt Lake City, UT, USA, 2008.

[18] Y. P. Chen, W. C. Chew, and L. Jiang, "A new green's function formulation for modeling homogeneous objects in layered medium," *IEEE Trans. Antennas Propag.*, vol. 60, no. 10, pp. 4766–4776, Oct. 2012.

[19] Y. P. Chen, L. Jiang, S. Sun, W. C. Chew, and J. Hu, "Calderón preconditioned PMCHWT equations for analyzing penetrable objects in layered medium," *IEEE Trans. Antennas Propag.*, vol. 62, no. 11, pp. 5619–5627, Nov. 2014.

[20] Y. Ren, Y. Chen, Q. Zhan, J. Niu, and Q. H. Liu, "A higher order hybrid SIE/FEM/SEM method for the flexible electromagnetic simulation in layered medium," *IEEE Trans. Geosci. Remote Sens.*, vol. 55, no. 5, pp. 2563–2574, May 2017.

[21] X. Millard and Q. H. Liu, "Simulation of near-surface detection of objects in layered media by the BCGS-FFT method," *IEEE Trans. Geosci. Remote Sens.*, vol. 42, no. 2, pp. 327–334, Feb. 2004.

[22] D. Alumbaugh and H. Morrison, "Electromagnetic conductivity imaging with an iterative Born inversion," *IEEE Trans. Geosci. Remote Sens.*, vol. 31, no. 4, pp. 758–763, Jul. 1993.

[23] Q.-H. Liu, "Nonlinear inversion of electrode-type resistivity measurements," *IEEE Trans. Geosci. Remote Sens.*, vol. 32, no. 3, pp. 499–507, May 1994.

[24] T. J. Cui, W. C. Chew, A. A. Aydiner, and S. Chen, "Inverse scattering of two-dimensional dielectric objects buried in a lossy earth using the distorted Born iterative method," *IEEE Trans. Geosci. Remote Sens.*, vol. 39, no. 2, pp. 339–346, Feb. 2001.

[25] L. H. Cox, G. A. Wilson, and M. S. Zhdanov, "3D inversion of airborne electromagnetic data," *Geophysics*, vol. 77, no. 4, pp. WB59–WB69, Jul. 2012.

[26] B. Liang *et al.*, "A new inversion method based on distorted born iterative method for grounded electrical source airborne transient electromagnetics," *IEEE Trans. Geosci. Remote Sens.*, vol. 56, no. 2, pp. 877–887, Feb. 2018.

[27] C. Qiu *et al.*, "Multifrequency 3-D inversion of GREATEM Data by BCGS-FFT-BIM," *IEEE Trans. Geosci. Remote Sens.*, vol. 57, no. 4, pp. 2439–2448, Apr. 2019.

[28] K. A. Michalski and J. R. Mosig, "Multilayered media Green's functions in integral equation formulations," *IEEE Trans. Antennas Propag.*, vol. 45, no. 3, pp. 508–519, Mar. 1997.

[29] T. J. Cui and W. C. Chew, "Fast algorithm for electromagnetic scattering by buried 3-D dielectric objects of large size," *IEEE Trans. Geosci. Remote Sens.*, vol. 37, no. 5, pp. 2597–2608, Sep. 1999.

[30] A. R. Sebak, L. Shafai, and Y. Das, "Near-zone fields scattered by three-dimensional highly conducting permeable objects in the field of an arbitrary loop," *IEEE Trans. Geosci. Remote Sens.*, vol. 29, no. 1, pp. 9–15, Jan. 1991.

[31] Z. Q. Zhang and Q. H. Liu, "Applications of the BCGS-FFT method to 3-D induction well-logging problems," *IEEE Trans. Geosci. Remote Sens.*, vol. 41, no. 5, pp. 998–1004, Jun. 2003.

[32] M. Moghaddam and W. C. Chew, "Nonlinear two-dimensional velocity profile inversion using time domain data," *IEEE Trans. Geosci. Remote Sens.*, vol. 30, no. 1, pp. 147–156, Jan. 1992.

[33] Z. Yu, J. Zhou, Y. Fang, Y. Hu, and Q. H. Liu, "Through-casing hydraulic fracture evaluation by induction logging II: The inversion algorithm and experimental validations," *IEEE Trans. Geosci. Remote Sens.*, vol. 55, no. 2, pp. 1189–1198, Feb. 2017.

[34] T. Eadie, J. M. Legault, G. Plastow, A. Prikhodko, and P. Tishin, "VTEM ET: An improved helicopter time-domain EM system for near surface applications," *ASEG Extended Abstr.*, vol. 2018, no. 1, pp. 1–5, Dec. 2018.

[35] C. Yin and D. C. Fraser, "Attitude corrections of helicopter EM data using a superposed dipole model," *Geophysics*, vol. 69, no. 2, pp. 431–439, Mar. 2004.

[36] A. P. Raiche, "Transient electromagnetic field computations for polygonal loops on layered earths," *Geophysics*, vol. 52, no. 6, pp. 785–793, Jun. 1987.

[37] J. A. Lehmann-Horn, M. Hertrich, S. A. Greenhalgh, and A. G. Green, "Three-dimensional magnetic field and NMR sensitivity computations incorporating conductivity anomalies and variable-surface topography," *IEEE Trans. Geosci. Remote Sens.*, vol. 49, no. 10, pp. 3878–3891, Oct. 2011.

[38] Y. Das, J. E. Mcfee, J. Toews, and G. C. Stuart, "Analysis of an electromagnetic induction detector for real-time location of buried objects," *IEEE Trans. Geosci. Remote Sens.*, vol. 28, no. 3, pp. 278–288, May 1990.

[39] L. Carin, H. Yu, Y. Dalichaouch, A. R. Perry, P. V. Czipott, and C. E. Baum, "On the wideband EMI response of a rotationally symmetric permeable and conducting target," *IEEE Trans. Geosci. Remote Sens.*, vol. 39, no. 6, pp. 1206–1213, Jun. 2001.

[40] Z. Zhao and J. C. West, "Low-grazing-angle microwave scattering from a three-dimensional spilling breaker crest: A numerical investigation," *IEEE Trans. Geosci. Remote Sens.*, vol. 43, no. 2, pp. 286–294, Feb. 2005.

Chen Qiu received the B.S. degree in electronic information science and technology and the M.A. degree in theoretical physics from the Xiamen University, Xiamen, China, in 2010 and 2013, respectively, where he is currently pursuing the Ph.D. degree.

His research interests include fast 3-D electromagnetic forward and inverse scattering algorithm as well as their applications in ATEM and GPR.

Bingyang Liang received the B.E. degree in communication engineering from the PLA Information Engineering University, Zhengzhou, China, in 2011, and the M.S. degree in electronics and communication engineering and the Ph.D. degree in electronic science from the Xiamen University, Xiamen, China, in 2014 and 2019, respectively.

His research interests include the forward and inversion method of electromagnetics and acoustics, as well as their applications in ATEM and photoacoustic tomography.

Feng Han (Member, IEEE) received the B.S. degree in electronic science from the Beijing Normal University, Beijing, China, in 2003, the M.S. degree in geo-physics from the Peking University, Beijing, in 2006, and the Ph.D. degree in electrical engineering from the Duke University, Durham, NC, USA, in 2011.

He is currently an Assistant Professor with the Institute of Electromagnetics and Acoustics, Xiamen University, Xiamen, China. His research interests include ionosphere remote sensing by radio atmospherics, electromagnetic full-wave inversion by integral equations, reverse time migration image, and the design of an electromagnetic detection system.

Jutao Li received the B.S. degree in electronic science from the Central South University, Hunan, China, in 1998, and the M.S. degree in communication engineering from the University of Chinese Academy of Sciences, Beijing, in 2012.

He is currently an Associate Professor with the Institute of Electronics, Chinese Academy of Sciences, Beijing. Since 2016, he has been the Deputy Director of the Key Lab of Electromagnetic Radiation and Sensing Technology of CAS. His research interests include electromagnetic field theory, ultrawideband radar, and geophysical electromagnetic exploration technology.

Guangyou Fang received the B.S. degree in electrical engineering from the Hunan University, Changsha, China, in 1984, and the M.S. and Ph.D. degrees in electrical engineering from the Xi'an Jiaotong University, Xi'an, China, in 1990 and 1996, respectively.

From 1990 to 1999, he was an Engineer, Associate Professor, and Professor with the China Research Institute of Radio wave Propagation, Qingdao, China. From 2000 to 2001, he was a Visiting Scholar with the University of Trieste and International Center for Science and High Technology, Italy. From 2001 to 2003, he was a Special Foreign Research Fellow of the Japan Society for Promotion of Science, working with the Prof. M. Sato with Tohoku University, Tohoku, Japan. He was the PI of CE-3 lunar penetrating radar. Since 2004, he has been a Professor with the Institute of Electronics of Chinese Academy of Sciences (IECAS), the Director of the Key Lab of Electromagnetic Radiation and Sensing Technology of CAS, and the Deputy Director of IECAS from 2013. He has authored or coauthored more than 300 articles in refereed journals and conference proceedings. His research interests include electromagnetic field theory, ultrawideband radar, ground-penetrating radar, lunar and mars exploration radar, geophysical electromagnetic exploration technology, and THz Imaging.

Qing Huo Liu (Fellow, IEEE) received the B.S. and M.S. degrees in physics from Xiamen University, Xiamen, China, and the Ph.D. degree in electrical engineering from the University of Illinois at Urbana–Champaign, Champaign, IL, USA.

From September 1986 to December 1988, he was a Research Assistant with the Electromagnetics Laboratory, University of Illinois at Urbana–Champaign, where he was a Post-Doctoral Research Associate from January 1989 to February 1990. He was a Research Scientist and the Program Leader with Schlumberger-Doll Research, Ridgefield, CT, USA, from 1990 to 1995. From 1996 to May 1999, he was an Associate Professor with New Mexico State University, Las Cruces, NM, USA. Since June 1999, he has been with Duke University, Durham, NC, USA, as a Professor of electrical and computer engineering. His research interests include computational electromagnetics and acoustics, inverse problems, and their application in nanophotonics, geophysics, biomedical imaging, and electronic packaging. He has published widely in these areas.

Dr. Liu is a Fellow of the Acoustical Society of America, Electromagnetics Academy, and the Optical Society of America. He received the 1996 Presidential Early Career Award for Scientists and Engineers (PECASE) from the White House, the 1996 Early Career Research Award from the Environmental Protection Agency, the 1997 CAREER Award from the National Science Foundation, the 2017 Technical Achievement Award, the 2018 Computational Electromagnetics Award from the Applied Computational Electromagnetics Society, the 2018 Harrington-Mittra Award in Computational Electromagnetics from the IEEE Antennas and Propagation Society, and the ECE Distinguished Alumni Award from the University of Illinois at Urbana–Champaign in 2018. He has served as an IEEE Antennas and Propagation Society Distinguished Lecturer, and as the Founding Editor-in-Chief for the IEEE JOURNAL ON MULTISCALE AND MULTIPHYSICS COMPUTATIONAL TECHNIQUES.